Negative Pressures and Spallation in Water Drops Subjected to Nanosecond Shock Waves

Claudiu A. Stan,[1,] Philip R. Willmott,[2,3] Howard A. Stone,[4] Jason E. Koglin,[2] Mengning Liang,[2] Andrew L. Aquila,[2] Joseph S. Robinson,[2] Karl L. Gumerlock,[2] Gabriel Blaj,[5] Raymond G. Sierra,[1] Sébastien Boutet,[2] Serge A. H. Guillet,[2] Robin H. Curtis,[2] Sharon L. Vetter,[2] Henrik Loos,[6] James L. Turner,[6] and Franz-Josef Decker[6]*

[1]Stanford PULSE Institute, SLAC National Accelerator Laboratory, Menlo Park, CA 94025, USA

[2]Linac Coherent Light Source, SLAC National Accelerator Laboratory, Menlo Park, CA 94025, USA

[3]Paul Scherrer Institute, CH-5232 Villigen, Switzerland

[4]Department of Mechanical and Aerospace Engineering, Princeton University, Princeton, NJ 08544, USA

[5]Technology Innovation Directorate, SLAC National Accelerator Laboratory, Menlo Park, CA 94025, USA

[6]Accelerator Directorate, SLAC National Accelerator Laboratory, Menlo Park, CA 94025, USA

Corresponding Author

* Email: cstan@slac.stanford.edu

This material is based upon work supported by the U.S. Department of Energy, Office of Science, Office of Basic Energy Sciences, under Contract No. DE-AC02-76SF00515.

ABSTRACT

Most experimental studies of cavitation in liquid water at negative pressures reported cavitation at tensions significantly smaller than those expected for homogeneous nucleation, suggesting that achievable tensions are limited by heterogeneous cavitation. We generated tension pulses with nanosecond rise times in water by reflecting cylindrical shock waves, produced by X-ray laser pulses, at the internal surface of drops of water. Depending on the X-ray pulse energy, a range of cavitation phenomena occurred, including the rupture and detachment, or spallation, of thin liquid layers at the surface of the drop. When spallation occurred, we evaluated that negative pressures below −100 MPa were reached in the drops. We model the negative pressures from shock reflection experiments using a nucleation-and-growth model that explains how rapid decompression could outrun heterogeneous cavitation in water, and enable the study of stretched water close to homogenous cavitation pressures.

TOC GRAPHICS

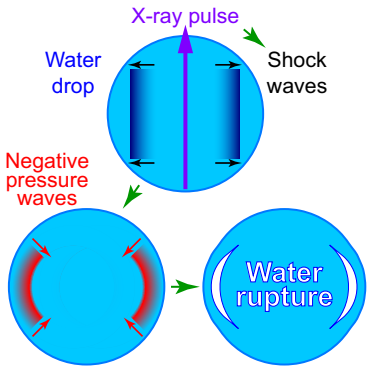

KEYWORDS

Stretched water, cavitation, heterogeneous nucleation, dynamic decompression, X-ray lasers

Liquid water can exist in states metastable relative to the vapor phase, either as a superheated liquid or as a liquid under tension (negative pressures).[1-3] While small volumes of pure water can be superheated to temperatures close to the homogenous boiling temperature,[4-5] most studies of cavitation in water near room temperature reported cavitation pressures down to −30 MPa,[2, 6-9] although homogeneous cavitation is expected to occur around −150 MPa.[10-12] To date, negative pressures below −100 MPa were only achieved using isochorically cooled water in mineral inclusions with dimensions on the order of 10 μm;[11, 13-16] the reason for which water cavitation is different in inclusions than in bulk remains unknown.[8-9] The apparent −30 MPa cavitation limit for bulk water is attributed to heterogeneous nucleation by intrinsic cavitation nuclei present in pure water.[7, 12]

Since nucleation occurs on a finite time scale, rapid decompression should allow the generation of lower negative pressures than in static experiments. Ultrasonic water cavitation experiments[7, 12, 17-18] can apply ~50 ns transient tensions, but reached only ~−30 MPa, far from homogenous cavitation pressures. A more rapid decompression can be achieved by reflecting shock waves at a free surface. The reflections can produce negative pressure waves with rapidly growing amplitudes,[19] which lead to spallation—the rupture of solids[20-21] or liquids[22-26] at a well-defined surface. Spallation experiments can determine the maximum negative pressure, or the tensile strength, that the material sustains during decompression.[20] Several spallation measurements in water have been performed to date,[27-30] with an experiment using millimeter-sized cells reporting negative pressures below −40 MPa.[29] A recent microfluidic cavitation experiment also used the reflection of shocks to stretch water; in this miniaturized setup, negative pressure pulses shorter than 10 ns reached −60 MPa before cavitation.[31]

Here, we report spallation in spherical microdrops of liquid water. Our experiment is illustrated in Figure 1A. We injected in a vacuum chamber microdrops of deionized water, synchronized such that they were intercepted by an ultrafast (30–40 fs) X-ray laser pulse[32] propagating perpendicularly to the direction of travel of the drops. The X-rays were focused to a beam size much smaller than the drop diameters, and passed through the center of the drops. We chose the X-ray photon energy (9.5 keV) and the drop diameters (55 and 71 μm) such that the X-rays were attenuated by a factor of less than 0.05 in a drop. Under these conditions, the X-rays deposit energy within a narrow filament with approximately the same diameter as the beam, and the energy density along the filament is approximately constant.[33] The X-rays deposited energy densities that are equivalent to filament pressures on the order of 100 GPa. The release of the filament pressure generates cylindrical shock waves inside the drop, and causes the explosion of the drop. For each interaction between a drop and an X-ray pulse, we imaged optically the drop, perpendicularly to both the drop motion and the X-ray beam, using pulsed illumination from a femtosecond laser.

The shock waves and the phase transition dynamics for different pulse energies are presented in Figure 1B. A more detailed illustration of the dynamics is available as movies (see Supporting Information (SI)). We will refer to the axis defined by the X-ray beam as the axis of the drop, and to the midsection perpendicular to this axis as the equatorial plane of the drop. In all experiments

shown in Figure 1B, we observed shock waves. They became visible at a distance of 5 to 7 µm from the beam axis approximately 1 ns after the X-ray pulse, and then propagated towards the surface of the drop with initial velocities around 2000 m/s. We also observed the formation of a central region that evolved into a cavity inside the drop. The shock waves later disappeared from view, and two wave fronts propagated from the poles of the drop back toward the center. These wave fronts are the first consequence of the reflection of the shock at the surface of the drop.

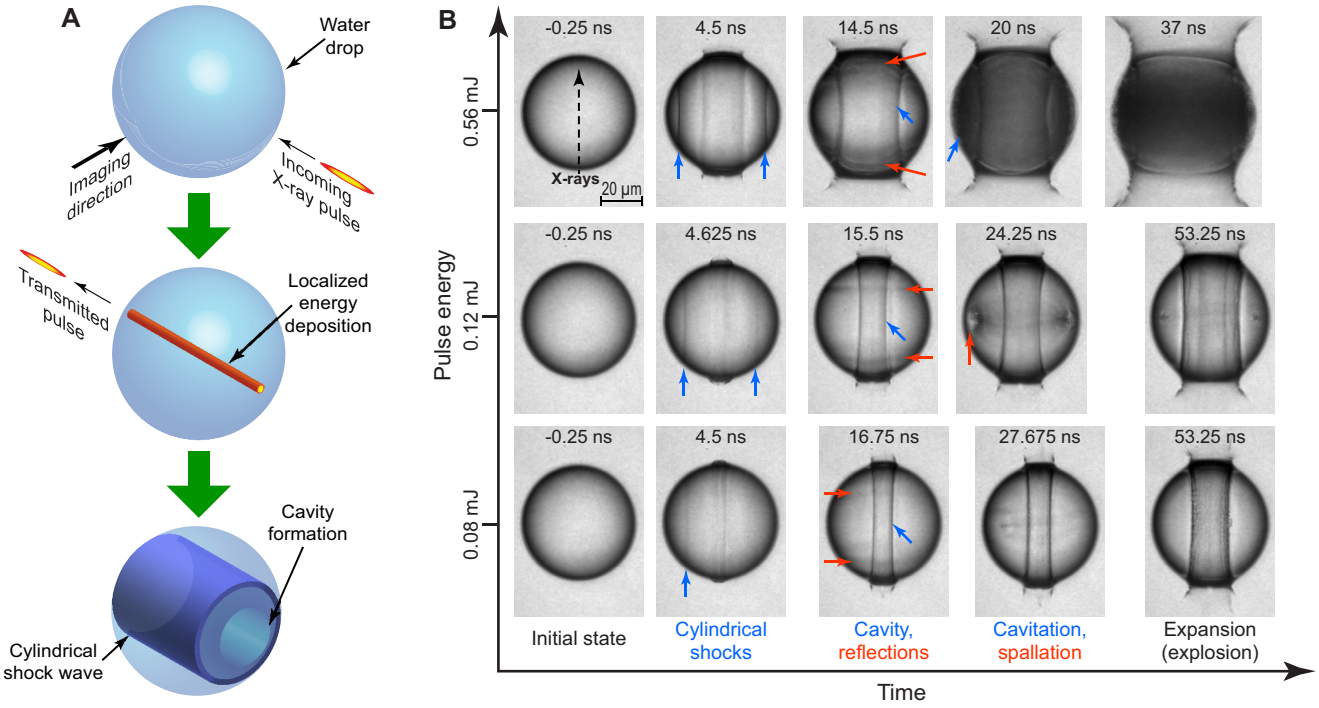

Figure 1. (A) Experimental design. A focused, ultra-intense X-ray laser pulse deposits energy in microdrops of water, forming a high-pressure filament that launches a shock wave and forms a cavity inside a drop. These processes are investigated using time-resolved, bright-field optical imaging. (B) Images of 55-µm diameter water drops during the experiments. For each column in the array of images, the solid arrows indicate the location of the phenomena listed at the bottom of the column, in the same font color as the arrows. The shock waves are visible as straight lines; they are reflected from the surface of the drops into negative pressure waves that can lead to cavitation or spallation inside the drop. Spallation produces a void-liquid interface that reflects the illumination light and leads to the appearance of bright regions in the images.

The reflection of a shock wave at a free surface generates a counter-propagating negative pressure wave,[19, 34] which will cause cavitation in liquids if sufficiently strong.[35] We observed random or no cavitation at low pulse energies (0.08 mJ, Figure 1B), and cavitation in the whole volume of the drop at high pulse energies (0.56 mJ). At intermediate pulse energies (0.12 mJ), the cavitation was localized near the equatorial plane, and was accompanied by the appearance of high-brightness areas in the cavitation region. The cavitation was localized because the spherical surface of the drop focuses the negative pressure wave. The high-brightness areas were dark when imaged through crossed optical polarizers, and therefore do not represent sonoluminiscence.[36-38] Instead, they most likely represent optically clear regions with low refractive index, such as voids caused by spallation.

We measured the shock wave pressures using the relation between the instantaneous pressure at the interface, $P(t)$, and the instantaneous velocity of the interface $v_i(t)$,[19]

$$P(t) = \frac{1}{2}\rho_0 c_S v_i(t) \qquad (1)$$

where t is the measurement time, and c_S and ρ_0 are, respectively, the shock velocity and the density of water. Since the reflected wave has a negative pressure with an absolute value equal to that of the shock, Eqn. (1) can be used to derive the pressure profiles of the shock and the reflected wave, and the time-dependent pressure distribution in the drop.

We determined the motion of the drop's surface in the equatorial plane through measurements of the diameter of the drop, performed with an edge detection algorithm (see SI). The time evolution of the diameter of the drops is shown in Figure 2. The drops started to expand when the shock arrived at the interface, then the rate of expansion slowed down, and then the rate of expansion increased again. Up to the time when the expansion rate increases again, the diameter data can be differentiated to measure $v_i(t)$ and, using Eqn. (1), $P(t)$. Later, the pressure of the shock cannot be determined by this method, because additional variations of the surface velocity are caused by either secondary reflections of the pressure waves (0.08 mJ), or by spallation inside the drop (0.12 and 0.56 mJ).

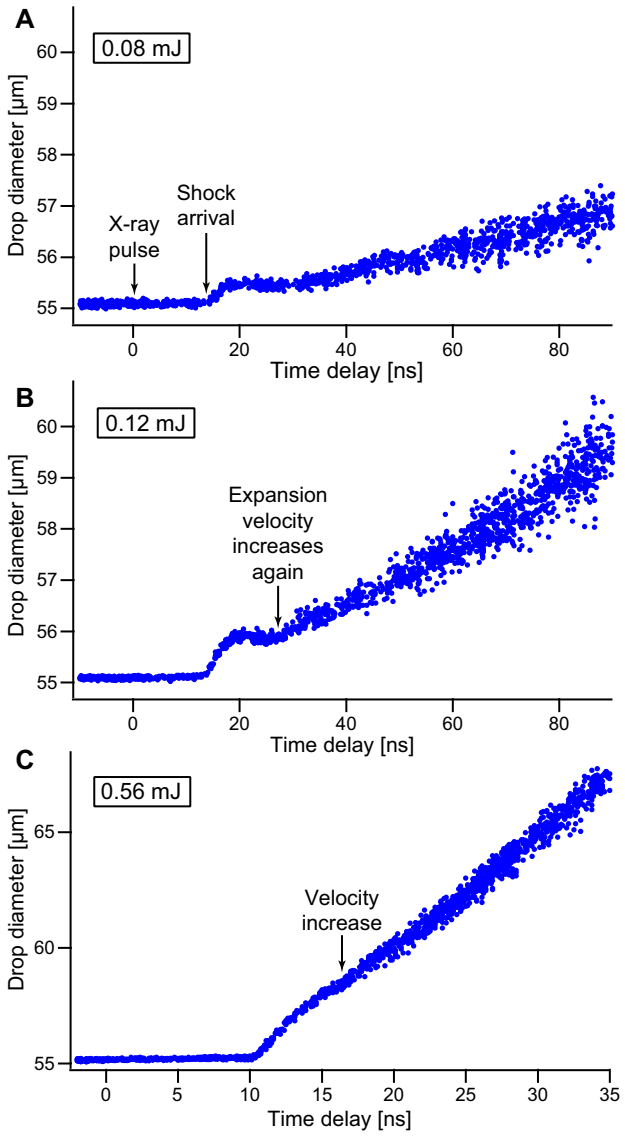

Figure 2. Evolution of the diameter of the drop in the equatorial plane. The diameter does not change until the shock arrives at the surface. The subsequent expansion of the drop occurs at a rate that increases with the pulse energy, and has variations related to the shock wave dynamics. (A) Diameter evolution when shock waves are generated, but spallation is not observed in the images of drops. (B) Diameter evolution near the pulse energy threshold for spallation, which causes an easily identifiable second increase in the expansion velocity. (C) Diameter evolution for high pulse energy. The change in the expansion velocity due to spallation becomes difficult to resolve against the background of a high expansion velocity.

The mechanism of spallation in the drops is illustrated in Figure 3A. The initial shock is reflected as a negative pressure wave whose amplitude increases until it reaches a maximum negative pressure; the water ruptures shortly thereafter, at the spall surface. The rupture generates a void, whose surface reflects part of the negative pressure wave into a radially outward, positive pressure wave. This twice-reflected wave arrives at the drop surface and causes the second increase in the interface velocity (Figure 2B). In the case of planar shocks reflected at planar interfaces, the maximum pressure P_{planar} can be evaluated using Eqn. (2), which approximates the velocity of all waves with the speed of sound c_0,[39-40]

$$P_{planar} = -\frac{1}{2}\rho_0 c_0 \left(V_1 - V_2\right) \quad (2)$$

where V_1 is the surface velocity just after the arrival of the shock (proportional to the pressure of the reflected wave at the spall plane) and V_2 is the interface velocity just before the second increase in surface velocity (proportional to the pressure in the trailing part of the shock at the spall plane). We measured V_1 and V_2 by fitting the evolution of the drop diameter, as shown in Figure 3B.

In our experiments, Eqn. (2) must be modified to include the focusing of the reflected wave by the spherical surface of the drop. We quantified the focusing using two amplification factors, C_1 and C_2, which assume geometric small-angle reflections, and that all waves propagate at the speed of sound without losses,

$$C_1 = \frac{R_d}{R_{spall}} \quad (3)$$

$$C_2 = \frac{R_d}{2R_{spall} - R_d} \quad (4)$$

where R_d is the initial drop radius, and R_{spall} the radial position of the spall surface (see Figure 3A and the SI). In particular, C_1 is the "equatorial plane" amplification, which applies to both the shock and the reflected wave, and C_2 the "axial" amplification, which applies only to the reflected wave. We determined the position of the spall surface from the travel time of the twice-reflected wave, assuming that it originates at R_{spall} when spallation is first observed in the drops (t_{Sint}; see Figure 3B), and arrives at the drop surface when the surface velocity increases again (t_{Sext}). With focusing, the maximum negative pressure generated in the drops, P_{spall}, is

$$P_{spall} = -\frac{1}{2}\rho_0 c_0 \left(C_1 C_2 V_1 - C_1 V_2\right) \quad (5)$$

We calculated P_{spall} only for experiments in which high-brightness areas were observed, and the edge of the drop maintained its optical contrast after spallation; the results are given in Table 1 and indicate $P_{spall} < -100$ MPa. Since the drops cool evaporatively in vacuum, we modeled

numerically the temperature distribution in the drop,[41] and in Eqn. (5) we used the density and the speed of sound for water at the temperature of the surface.

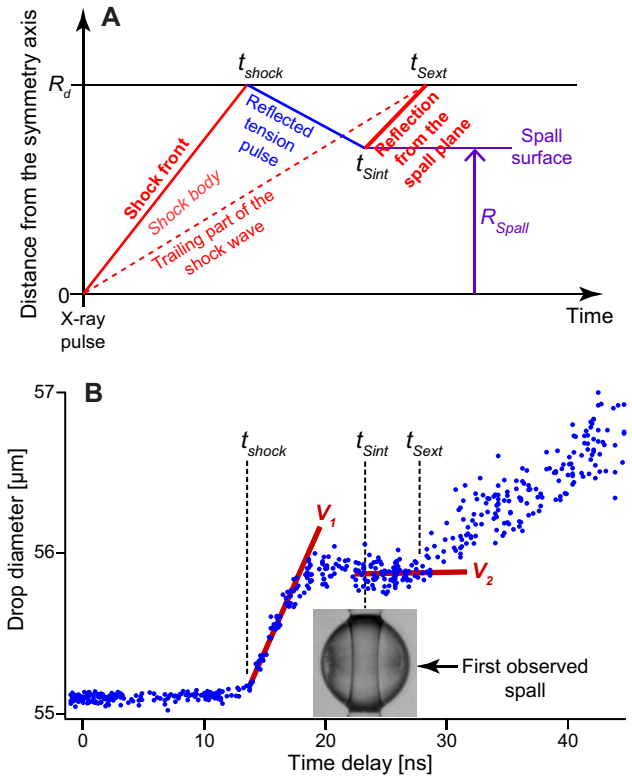

Figure 3. Spallation mechanism and its characterization. (A) Time-space schematic. Spallation is caused by the reflected negative pressure wave, and generates a spall surface that reflects the negative pressure wave. (B) Diameter measurements when spallation occurred. The key velocities and delay times can be determined from the images and the diameter data. The time axes in panels (A) and (B) are aligned to help identify the spallation parameters.

Table 1. Experimental results.[a]

Data set	Drop radius [μm]	Pulse energy [μJ]	V_1 [m/s]	V_2 [m/s]	R_{spall} [μm]	Temperature at surface [°C]	Temperature at R_{spall} [°C]	C_1	C_2	P_{spall} [MPa]
1	27.6±0.1	120±3	86±5	1±2	21±1	−6.1±0.7	5.0±1.1	1.3±0.1	1.9±0.3	−146±34[b]
2	35.7±0.1	118±6	56±7	2±3	25±2	−7.0±0.7	9.7±1.2	1.4±0.1	2.6±0.5	−137±41[b]
3	35.7±0.1	166±8	78±11	0±4	26±1	−7.0±0.7	8.0±1.2	1.3±0.1	2.1±0.2	−152±35[b]

[a]The diameter data for set 1 is displayed in Figures 1B and 2B. The diameter data for sets 2 and 3 is available in the SI. The error differentials are standard deviations (drop radii, surface velocities V_1 and V_2), spread of data (pulse energies), or estimated uncertainties for the rest of the parameters (temperatures, C_1, C_2, P_{Spall}). C_1, C_2, and P_{Spall} are defined in Eqs. (3), (4), and (5), respectively. [b]The uncertainty of P_{Spall} was calculated by propagating the error differentials of V_1, V_2, and R_{Spall}, assuming that they are independent variables.

Our experiment is distinguished from previous spallation experiments by the focusing of the reflected wave, which amplifies several-fold the negative pressure. The focusing of shock reflections inside free water drops was observed previously,[42] but this phenomenon is mostly unexplored. The amplification factors C_1 and C_2 represent a first-order approximation of shock wave reflections, and may overestimate the negative pressures given in Table 1. Therefore, we cannot conclude that spallation occurred through homogeneous nucleation. Instead, our results show that negative pressures below −100 MPa could be achieved in bulk water, *despite heterogeneous cavitation*.

The large negative pressures we observed are primarily due to rapid decompression times (~2 ns) from zero pressure to P_{Spall}, shorter than achieved previously.[17, 29, 31] Shorter decompression times lead to larger negative pressures, and previous studies reported changes of several MPa in the cavitation pressure of water when the decompression times were decreased by a factor of ~2.[17, 29] This dependence was explained using cavitation models based on nucleation kinetics.[17, 29] These models fail to explain the combined measurements of Bogach and Utkin,[29] Ando *et al.*,[31] and ours, which indicate that as decompression times decrease from ~20 ns to ~2 ns, the negative pressures increase from ~−40 MPa to below −100 MPa.

The negative pressures we observed (Table 1) can be explained by taking into account both the nucleation and the growth of cavitation bubbles. Nucleation-and-growth models have been applied previously to the problem of dynamic tensile failure in solids and liquids[40, 43-45] and it was found[45] that the growth of voids can be modeled using the Rayleigh-Plesset equation,[46]

$$-\frac{(P_{ext}-P_b)}{\rho}=R\frac{d^2R}{dt^2}+\frac{3}{2}\left(\frac{dR}{dt}\right)^2+\frac{4\eta}{\rho R}\frac{dR}{dt}+\frac{2\sigma}{\rho R} \qquad (6)$$

where R is the bubble radius, P_{ext} the pressure in the liquid, P_b the pressure inside the bubble, and ρ, η and σ are, respectively, the density, viscosity, and surface tension of the liquid.

We modeled the cavitation that leads to spallation using separate stages of heterogeneous cavitation and bubble growth. Heterogeneous cavitation nuclei in water have been proposed to be either (i) nuclei with a lower surface tension than water (type-I) or (ii) stabilized nanobubbles that start to grow below a threshold pressure (type-II).[7] Ultrasonic cavitation experiments that reached negative pressures around −30 MPa can be explained by type-I nuclei.[7] Our model, which applies to larger negative pressures, assumes instead the existence of a fixed concentration of type-II nuclei that nucleate at a threshold pressure near −30 MPa.

Our model of the dynamic decompression is illustrated in Figure 4A. A volume of water initially at room temperature and zero pressure is stretched at a constant rate until the water, in the absence of cavitation, would approach the liquid-vapor spinodal density, ~900 kg/m^3, predicted by extrapolating[3, 18] the IAWPS equation of state for water.[47] A fixed concentration of type-II nuclei is present in water, and all nuclei start to grow as bubbles once the threshold negative pressure is reached. The growth of bubbles reduces the tension in the stretched water, but since the rate of growth of bubbles is finite, the tension is only partially relaxed during the decompression. We integrated numerically the Rayleigh-Plesset equation (Eqn. (6)) to calculate the bubble volume, and the pressure in the liquid phase (see SI).

As an example of this model, the evolution of the negative pressure for a nuclei concentration of 10^{-10} mol/L and a decompression time of 4 ns is shown in Figure 4B. The pressure in the liquid initially follows the one expected in the absence of cavitation, then reaches a minimum pressure, and then increases. In our model, the negative pressure depends primarily on the nuclei concentration and on the decompression time. Figure 4C shows the maximum negative pressures given by our model for a range of decompression times and for several nuclei concentrations, along with experimental measurements,[29, 31] and a prediction of the cavitation pressures according to a nucleation-only model.[17] To obtain the experimental values, we selected and interpreted the published data (see Experimental Methods),[29, 31] and we evaluated the decompression time as the rise time of the negative pressure wave (see SI).

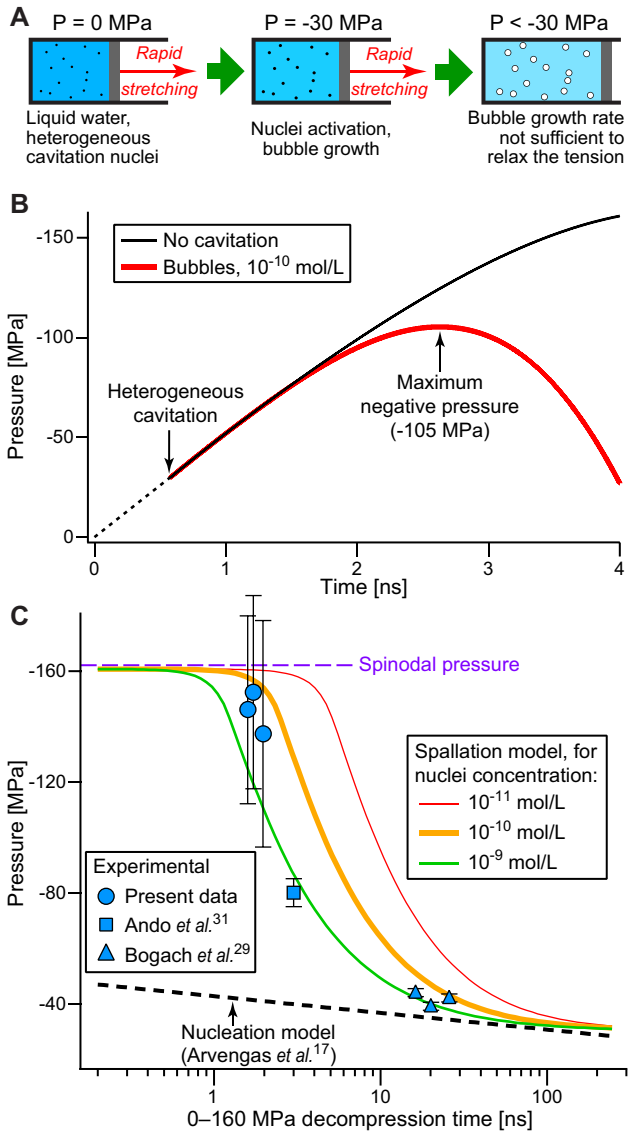

Figure 4. (a) Nucleation-and-growth model. Heterogeneous cavitation occurs at −30 MPa at preexisting nuclei and is followed by bubble growth, which reduces the negative pressures but not completely. (b) Modeled negative pressures if bubbles grow, and if cavitation is absent. The negative pressure in the liquid reaches a limit if bubbles grow. (c) Maximum negative pressures predicted by the model for different nuclei concentrations, experimental measurements, and an extrapolation of cavitation pressures from ultrasonic studies. The maximum negative pressures approach rapidly the spinodal pressure in liquid water as the decompression times become shorter than ~10 ns.

Our dynamic two-phase model provides a better explanation of the maximum negative pressures than nucleation-only methods, but given the limited number of experiments that reported pressures significantly below −30 MPa, we cannot rule out a more complex process of nucleation and growth. Our analysis highlights the importance of bubble growth during dynamic decompression and the possibility of multiple heterogeneous cavitation mechanisms in water, and suggests that nucleation-and-growth models can connect spallation experiments with cavitation experiments that detect the nucleation of single bubbles. In particular, such models may explain the big spread of negative pressures reported by microfluidic shock reflection experiments.[31, 48-49]

Just as significantly, the measurements in Figure 4C are consistent with a nuclei concentration between 10^{-9} and 10^{-10} mol/L. This concentration is 2–3 orders of magnitude lower than the concentration of hydronium ions, which may be related to the heterogeneous cavitation nuclei in water.[12] If water contains intrinsic type-II nuclei at this concentration, the bubble growth at large tensions is inertial,[46] and we can estimate analytically the 100%–90% decay time, t_{90}, of a suddenly applied negative pressure P_{neg} due to cavitation (see SI)

$$t_{90} = 0.353 \frac{\sqrt{\rho_0}}{\mathrm{K}^{1/3}} \frac{1}{|P_{neg}|^{1/6}} \frac{1}{n_c^{1/3}} \qquad (7)$$

where K is the bulk modulus of water and n_c the concentration of nuclei. Eqn. (7) predicts that large negative pressures can be sustained for ~1 ns in water.

The possibility of stretching water to achieve pressures below −100 MPa, through decompression in less than a few nanoseconds, opens new possibilities for the study of stretched water. For example, decompression of supercooled water produces doubly metastable water.[16, 50] Our experiments were performed close to the melting curve expected at negative pressures,[13, 16] and can be extended to deeply doubly-metastable conditions. Nanosecond decompression times are long enough to study the properties of stretched water through time-resolved optical spectroscopy,[51-53] and with X-ray lasers.[54-55] In particular, multi-pulse X-ray laser techniques[56-57] could enable experiments in which stretched water is both produced and studied using ultra-intense X-ray pulses.

EXPERIMENTAL METHODS

We used deionized water supplied by a water purification system (Milli-Q Integral, EMD Millipore). During handling and injection, water came in contact with polypropylene, polyetheretherketone (PEEK), stainless steel, and silica surfaces. All recipients, tubing and injectors have been only used with pure water since purchased, and were thoroughly rinsed and multiply flushed before the experiments.

The drops were produced by triggering the Rayleigh capillary breakup of free jets, using piezoelectric drop injectors (MJ-AT series, MicroFab Inc.) with orifice diameters of 25 and 30 μm to make drops with diameters of 55 and 71 μm, respectively. The electrical signal to the injector was synchronized electronically with the X-ray pulse timing signal to ensure that each X-ray pulse passed through the center of one drop.

The experiments were conducted at the Coherent X-ray Imaging instrument (CXI)[58] at the Linac Coherent Light Source (LCLS),[32] using self-amplified spontaneous emission X-ray pulses of 9.5 keV photons with a duration from 30 to 40 fs, and a total pulse energy up to ~1 mJ arriving at the drops. The X-ray beam was focused using a Kirkpatrick-Baez mirror system[59] to a spot size of ~1 μm full width at half maximum (FWHM). The measurements were conducted as experimental "runs" in which the pulse energy and the drop diameter were constant, but the time delay between the X-rays and the optical imaging was varied to determine the dynamics induced by X-rays. Within a run, we acquired data at the repetition rate of the X-ray laser, 120 measurements (or "shots") per second. This experimental setup is based on the design we used previously to investigate explosions induced by X-ray laser pulses in liquid jets and drops,[33] but was upgraded to image the drops at higher spatial and temporal resolutions.

The imaging system is based on a 50X long-working distance objective (Mitutoyo) with a 200-mm focal length tube lens, and has an optical resolution better than 780 nm when imaging resolution test targets (USAF 1951 pattern, Edmund Optics). We recorded images with a magnification of 200 nm/pixel using a high-speed camera (Phantom Miro M340, Vision Research). We used pulsed illumination from a 800-nm femtosecond laser (Legend Elite, Coherent Inc.); the light pulses were decompressed temporally to ~100 ps duration to avoid damage to the optical components, and then decohered by passing them through a diffuser (600 grit size, ThorLabs) and an optical fiber bundle (1/8" diameter, Edmund Optics). The imaging light was linearly polarized, with the polarization axis along the X-ray direction. The delay between the X-ray pulses and the imaging light pulses was varied from shot to shot by scanning the position of the delay stage of the femtosecond laser, and was measured with a fast photodiode whose signal was recorded by a fast digitizer (Acqiris 1065A, Keysight Technologies). The temporal resolution of the imaging setup was given by the time acquisition window of the digitizer, 125 ps, and the temporal accuracy of measurements was ~250 ps.

The data collected in an experimental run did not correspond to identical conditions of interaction between the X-ray pulses and the drops, because of X-ray pulse energy jitter, and of mechanical vibrations that affected the alignment between the X-rays and the center of the drops.

For spallation measurements, we selected from the raw data shots in which the X-ray pulse was aligned to the center of the drop, and in which the energy of the pulses fell within a narrow band around the mean pulse energy. The width of the pulse energy band (5% to 10% of the mean value) was chosen such that enough data points were available to calculate the parameters of spallation.

The data from literature included in Figure 4C was selected and interpreted as follows. Instead of using the cavitation pressure reported by Ando *et al.*[31] (−60 MPa), we deduced a spallation pressure of ~−80 MPa from the pressure contour enclosing the area in which cavitation bubbles were fully overlapping each other (see Figure 3(c) in their paper); we made this choice because spallation in water should generate on the order of one bubble per cubic micron, and thus darken completely the spall region in their optical images. From the nine experiments reported by Bogach and Utkin,[29] we selected for display in Figure 4C experiments 2, 6 and 7, which were performed with distilled water, and for which the interface velocimetry curves were noise-free and allowed us to estimate of the depth at which the spall occurred (see Table 1 and Figure 2 in their paper).

ASSOCIATED CONTENT

Supporting Information. The following files are available free of charge.

Additional information about (a) the detachment of liquid layers after spallation, (b) the generation of negative pressures through shock reflections, (c) the calculation of decompression times, (d) the nucleation-and-growth model of spallation, (e) the edge detection algorithm for diameter measurements, (f) the drop temperatures during evaporative cooling, (g) diameter data for spallation experiments in 71-µm diameter drops, and (h) the processing of supporting videos (PDF).

Five movies of shock waves and spallation in water drops (MOV).

AUTHOR INFORMATION

Notes

The authors declare no competing financial interests.

ACKNOWLEDGMENT

The work was primarily supported by the U.S. Department of Energy, Office of Science, Chemical Sciences, Geosciences, and Biosciences Division. Use of the Linac Coherent Light Source (LCLS), SLAC National Accelerator Laboratory, is supported by the U.S. Department of Energy, Office of Science, Office of Basic Energy Sciences under Contract no. DE-AC02-76SF00515. We thank Zhirong Huang for advice on the operation and capabilities of LCLS, Veit Elser for discussions, and Shibom Basu for experimental assistance.

REFERENCES

(1) Debenedetti, P. G. *Metastable Liquids: Concepts and Principles*, Princeton University Press: Princeton, NJ, 1997.

(2) Caupin, F. Escaping the No Man's Land: Recent Experiments on Metastable Liquid Water. *J. Non-Cryst. Solids* **2015,** *407*, 441-448.

(3) Meadley, S. L.; Angell, C. A. Water and Its Relatives: The Stable, Supercooled and Particularly the Stretched Regimes, In *" Water: Fundamentals as the Basis for Understanding the Environment and Promoting Technology"*, Proceedings of the International School of Physics "Enrico Fermi", Course 187, Varenna on Lake Como, Italy, July 8-13, 2013; Debenedetti, P. G.; Ricci, M. A.; Bruni, F., Eds. IOS Press: Amsterdam, The Netherlands, 2015; pp 19-43.

(4) Apfel, R. E. Water Superheated to 279.5 °C at Atmospheric Pressure. *Nature (London), Phys. Sci.* **1972,** *238*, 63-64.

(5) Avedisian, C. T. The Homogeneous Nucleation Limits of Liquids. *J. Phys. Chem. Ref. Data* **1985,** *14*, 695-729.

(6) Trevena, D. Cavitation and the Generation of Tension in Liquids. *J. Phys. D: Appl. Phys.* **1984,** *17*, 2139-2164.

(7) Herbert, E.; Balibar, S.; Caupin, F. Cavitation Pressure in Water. *Phys. Rev. E* **2006,** *74*, 041603.

(8) Caupin, F.; Herbert, E. Cavitation in Water: A Review. *C. R. Phys.* **2006,** *7*, 1000-1017.

(9) Caupin, F.; Arvengas, A.; Davitt, K.; Azouzi, M. E. M.; Shmulovich, K. I.; Ramboz, C.; Sessoms, D. A.; Stroock, A. D. Exploring Water and Other Liquids at Negative Pressure. *J. Phys.: Condens. Matter* **2012,** *24*, 284110.

(10) Fisher, J. C. The Fracture of Liquids. *J. Appl. Phys.* **1948,** *19*, 1062-1067.

(11) Zheng, Q.; Durben, D.; Wolf, G.; Angell, C. Liquids at Large Negative Pressures: Water at the Homogeneous Nucleation Limit. *Science* **1991,** *254*, 829-832.

(12) Davitt, K.; Arvengas, A.; Caupin, F. Water at the Cavitation Limit: Density of the Metastable Liquid and Size of the Critical Bubble. *Europhys. Lett.* **2010,** *90*, 16002.

(13) Roedder, E. Metastable Superheated Ice in Liquid-Water Inclusions under High Negative Pressure. *Science* **1967,** *155*, 1413-1417.

(14) Shmulovich, K. I.; Mercury, L.; Thiery, R.; Ramboz, C.; El Mekki, M. Experimental Superheating of Water and Aqueous Solutions. *Geochim. Cosmochim. Acta* **2009,** *73*, 2457-2470.

(15) Azouzi, M. E. M.; Ramboz, C.; Lenain, J.-F.; Caupin, F. A Coherent Picture of Water at Extreme Negative Pressure. *Nat. Phys.* **2013,** *9*, 38-41.

(16) Pallares, G.; Azouzi, M. E. M.; González, M. A.; Aragones, J. L.; Abascal, J. L.; Valeriani, C.; Caupin, F. Anomalies in Bulk Supercooled Water at Negative Pressure. *Proc. Natl. Acad. Sci. U.S.A.* **2014,** *111*, 7936-7941.

(17) Arvengas, A.; Davitt, K.; Caupin, F. Fiber Optic Probe Hydrophone for the Study of Acoustic Cavitation in Water. *Rev. Sci. Instrum.* **2011,** *82*, 034904.

(18) Davitt, K.; Rolley, E.; Caupin, F.; Arvengas, A.; Balibar, S. Equation of State of Water under Negative Pressure. *J. Chem. Phys.* **2010,** *133*, 174507.

(19) Zel'dovich, Y. B.; Raizer, Y. P. *Physics of Shock Waves and High-Temperature Hydrodynamic Phenomena*, 1st ed.; Academic Press: Waltham, MA, 1968.

(20) Meyers, M. A.; Aimone, C. T. Dynamic Fracture (Spalling) of Metals. *Prog. Mater. Sci.* **1983,** *28*, 1-96.

(21) Tamura, H.; Kohama, T.; Kondo, K.; Yoshida, M. Femtosecond-Laser-Induced Spallation in Aluminum. *J. Appl. Phys.* **2001,** *89*, 3520-3522.

(22) Carlson, G.; Henry, K. Technique for Studying Dynamic Tensile Failure in Liquids: Application to Glycerol. *J. Appl. Phys.* **1973,** *44*, 2201-2206.

(23) Carlson, G.; Levine, H. Dynamic Tensile Strength of Glycerol. *J. Appl. Phys.* **1975,** *46*, 1594-1601.

(24) Carlson, G. Dynamic Tensile Strength of Mercury. *J. Appl. Phys.* **1975,** *46*, 4069-4070.

(25) De Rességuier, T.; Signor, L.; Dragon, A.; Boustie, M.; Roy, G.; Llorca, F. Experimental Investigation of Liquid Spall in Laser Shock-Loaded Tin. *J. Appl. Phys.* **2007,** *101*, 013506.

(26) Utkin, A. V.; Sosikov, V. A.; Bogach, A. A.; Fortov, V. E. Tension of Liquids by Shock Waves. *AIP Conf. Proc.* **2004,** *706*, 765-768.

(27) Marston, P.; Pullen, G. Cavitation in Water Induced by the Reflection of Shock Waves. *AIP Conf. Proc.* **1982,** *78*, 515-519.

(28) Boteler, J.; Sutherland, G. Tensile Failure of Water Due to Shock Wave Interactions. *J. Appl. Phys.* **2004,** *96*, 6919-6924.

(29) Bogach, A.; Utkin, A. Strength of Water under Pulsed Loading. *J. Appl. Mech. Tech. Phys.* **2000,** *41*, 752-758.

(30) Bannikova, I.; Uvarov, S.; Bayandin, Y. V.; Naimark, O. An Experimental Study of Non-Newtonian Properties of Water under Electroexplosive Loading. *Tech. Phys. Lett.* **2014,** *40*, 766-768.

(31) Ando, K.; Liu, A.-Q.; Ohl, C.-D. Homogeneous Nucleation in Water in Microfluidic Channels. *Phys. Rev. Lett.* **2012,** *109*, 044501.

(32) Emma, P.; Akre, R.; Arthur, J.; Bionta, R.; Bostedt, C.; Bozek, J.; Brachmann, A.; Bucksbaum, P.; Coffee, R.; Decker, F. J.; et al. First Lasing and Operation of an Ångstrom-Wavelength Free-Electron Laser. *Nat. Photonics* **2010,** *4*, 641-647.

(33) Stan, C. A.; Milathianaki, D.; Laksmono, H.; Sierra, R. G.; McQueen, T. A.; Messerschmidt, M.; Williams, G. J.; Koglin, J. E.; Lane, T. J.; Hayes, M. J.; et al. Liquid Explosions Induced by X-Ray Laser Pulses. *Paper under review*, 2016.

(34) Henderson, L. On the Refraction of Shock Waves. *J. Fluid Mech.* **1989,** *198*, 365-386.

(35) Couzens, D.; Trevena, D. Critical Tension in a Liquid under Dynamic Conditions of Stressing. *Nature* **1969,** *222*, 473-474.

(36) Gaitan, D. F.; Crum, L. A.; Church, C. C.; Roy, R. A. Sonoluminescence and Bubble Dynamics for a Single, Stable, Cavitation Bubble. *J. Acoust. Soc. Am.* **1992,** *91*, 3166-3183.

(37) McNamara, W. B.; Didenko, Y. T.; Suslick, K. S. Sonoluminescence Temperatures During Multi-Bubble Cavitation. *Nature* **1999,** *401*, 772-775.

(38) Brenner, M. P.; Hilgenfeldt, S.; Lohse, D. Single-Bubble Sonoluminescence. *Rev. Mod. Phys.* **2002,** *74*, 425-484.

(39) Cochran, S.; Banner, D. Spall Studies in Uranium. *J. Appl. Phys.* **1977,** *48*, 2729-2737.

(40) Dekel, E.; Eliezer, S.; Henis, Z.; Moshe, E.; Ludmirsky, A.; Goldberg, I. Spallation Model for the High Strain Rates Range. *J. Appl. Phys.* **1998,** *84*, 4851-4858.

(41) Smith, J. D.; Cappa, C. D.; Drisdell, W. S.; Cohen, R. C.; Saykally, R. J. Raman Thermometry Measurements of Free Evaporation from Liquid Water Droplets. *J. Am. Chem. Soc.* **2006,** *128*, 12892-12898.

(42) Avila, S. R. G.; Ohl, C.-D. Cavitation-Induced Fragmentation of an Acoustically-Levitated Droplet. *J. Phys.: Conf. Ser.* **2015,** *656*, 012017.

(43) Curran, D. R.; Seaman, L.; Shockey, D. A. Dynamic Failure in Solids. *Phys. Today* **1977,** *30*, 46-55.

(44) Curran, D.; Seaman, L.; Shockey, D. Dynamic Failure of Solids. *Phys. Rep.* **1987,** *147*, 253-388.

(45) Kuksin, A. Y.; Norman, G.; Pisarev, V.; Stegailov, V.; Yanilkin, A. Theory and Molecular Dynamics Modeling of Spall Fracture in Liquids. *Phys. Rev. B* **2010,** *82*, 174101.

(46) Plesset, M. S.; Prosperetti, A. Bubble Dynamics and Cavitation. *Annu. Rev. Fluid Mech.* **1977,** *9*, 145-185.

(47) Wagner, W.; Pruß, A. The IAPWS Formulation 1995 for the Thermodynamic Properties of Ordinary Water Substance for General and Scientific Use. *J. Phys. Chem. Ref. Data* **2002,** *31*, 387-535.

(48) Quinto-Su, P. A.; Ando, K. Nucleating Bubble Clouds with a Pair of Laser-Induced Shocks and Bubbles. *J. Fluid Mech.* **2013,** *733*, R3.

(49) Li, Z.; Xiong, S.; Chin, L.; Ando, K.; Zhang, J.; Liu, A. Water's Tensile Strength Measured Using an Optofluidic Chip. *Lab Chip* **2015,** *15*, 2158-2161.

(50) Angell, C. A. Supercooled Water: Two Phases? *Nat. Mater.* **2014,** *13*, 673-675.

(51) Fecko, C.; Eaves, J.; Loparo, J.; Tokmakoff, A.; Geissler, P. Ultrafast Hydrogen-Bond Dynamics in the Infrared Spectroscopy of Water. *Science* **2003,** *301*, 1698-1702.

(52) Bakker, H.; Skinner, J. Vibrational Spectroscopy as a Probe of Structure and Dynamics in Liquid Water. *Chem. Rev.* **2009,** *110*, 1498-1517.

(53) Deàk, J. C.; Rhea, S. T.; Iwaki, L. K.; Dlott, D. D. Vibrational Energy Relaxation and Spectral Diffusion in Water and Deuterated Water. *J. Phys. Chem. A* **2000,** *104*, 4866-4875.

(54) Sellberg, J. A.; Huang, C.; McQueen, T. A.; Loh, N. D.; Laksmono, H.; Schlesinger, D.; Sierra, R. G.; Nordlund, D.; Hampton, C. Y.; Starodub, D.; et al. Ultrafast X-Ray Probing of Water Structure Below the Homogeneous Ice Nucleation Temperature. *Nature* **2014,** *510*, 381-384.

(55) Sellberg, J. A.; McQueen, T. A.; Laksmono, H.; Schreck, S.; Beye, M.; DePonte, D. P.; Kennedy, B.; Nordlund, D.; Sierra, R. G.; Schlesinger, D.; et al. X-Ray Emission Spectroscopy of Bulk Liquid Water in "No-Man's Land". *J. Chem. Phys.* **2015,** *142*, 044505.

(56) Decker, F.; Akre, R.; Brachmann, A.; Ding, Y.; Dowell, D.; Emma, P.; Fisher, A.; Frisch, J.; Gilevich, S.; Hering, P. A Demonstration of Multi-Bunch Operation in the LCLS, In *Proceedings of the 32nd International Free Electron Laser Conference*, FEL 2010, Malmö, Sweden, Aug 23-27, 2010; Joint Accelerator Conferences Website (JACoW): 2011; WEBP33, pp 467-470.

(57) Marinelli, A.; Ratner, D.; Lutman, A. A.; Turner, J.; Welch, J.; Decker, F. J.; Loos, H.; Behrens, C.; Gilevich, S.; Miahnahri, A. A.; et al. High-Intensity Double-Pulse X-Ray Free-Electron Laser. *Nat. Commun.* **2015,** *6*, 7369.

(58) Liang, M.; Williams, G. J.; Messerschmidt, M.; Seibert, M. M.; Montanez, P. A.; Hayes, M.; Milathianaki, D.; Aquila, A.; Hunter, M. S.; Koglin, J. E. ; et al. The Coherent X-Ray Imaging Instrument at the Linac Coherent Light Source. *J. Synchrotron Radiat.* **2015,** *22*, 514-519.

(59) Siewert, F.; Buchheim, J.; Boutet, S.; Williams, G. J.; Montanez, P. A.; Krzywinski, J.; Signorato, R. Ultra-Precise Characterization of LCLS Hard X-Ray Focusing Mirrors by High Resolution Slope Measuring Deflectometry. *Opt. Express* **2012,** *20*, 4525-4636.